

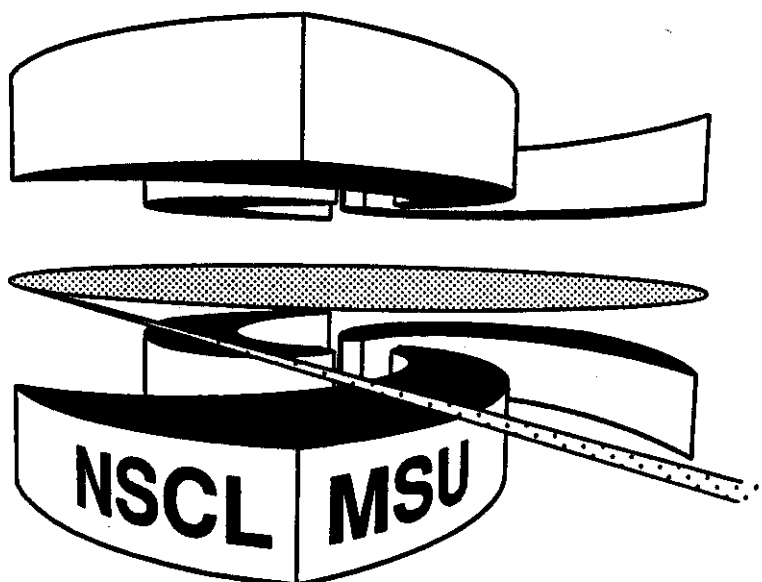


Michigan State University

National Superconducting Cyclotron Laboratory

**IMPACT PARAMETER FILTERS FOR  $^{36}\text{Ar} + ^{197}\text{Au}$   
COLLISIONS AT E/A = 50, 80, AND 110 MeV**

**L. PHAIR, D.R. BOWMAN, C.K. GELBKE, W.G. GONG,  
Y.D. KIM, M.A. LISA, W.G. LYNCH, G.F. PEASLEE,  
R.T. de SOUZA, M.B. TSANG, and F. ZHU**



# Impact parameter filters for $^{36}\text{Ar}+^{197}\text{Au}$ collisions at $E/A=50, 80, \text{ and } 110 \text{ MeV}$

*L. Phair, D.R. Bowman, C.K. Gelbke,*  
*W.G. Gong,<sup>†</sup> Y.D. Kim,\* MA. Lisa, W.G. Lynch,*  
*G.F. Peaslee, R.T. de Souza,\* M.B. Tsang, and F. Zhu*

National Superconducting Cyclotron Laboratory  
and Department of Physics and Astronomy  
Michigan State University, East Lansing, MI 48824, USA

**Abstract:** Collisions between  $^{36}\text{Ar}$  projectiles and  $^{197}\text{Au}$  target nuclei at  $E/A=50, 80, \text{ and } 110 \text{ MeV}$  have been studied with the MSU Miniball, a 4x phoswich array with a low detection threshold. Various impact parameter filters, based upon total charged-particle multiplicity, transverse energy, mid-rapidity charge and multiplicity of emitted hydrogen nuclei, are compared and **cross-correlated**. The relative selectivity of each prescription for small impact parameter collisions is evaluated by assessing the suppression of fast particle emission at forward angles.

PACS index: **25.70.Np**

## I. Introduction

Still today, it is not yet clear how experimental observables from nuclear collision experiments can provide quantitative information about phase transitions in nuclear matter [1-13] - whether it is a liquid-gas phase transition at moderate temperatures and low densities, or a transition between a nucleon gas and a quark-gluon plasma at high densities and temperatures.

Intermediate energy nucleus-nucleus collisions may produce finite nuclear systems at temperatures and densities commensurate with a liquid-gas phase transition in infinite nuclear matter. However, interpretations of inclusive measurements are complicated by the implicit average over impact parameter which makes it difficult to unravel the complex interplay between statistical and dynamical effects. Comparisons between experiment and theory are expected to become more tractable and more sensitive to unknown model parameters as research becomes more focussed upon exclusive experiments in which specific reaction filters are employed to select narrow ranges of impact parameter.

In most experiments, information about the impact parameter is extracted from quantities which relate to the collision geometry via simple intuitive pictures. Many impact parameter filters represent some measure of the "violence" of the reaction which, in turn, is assumed to be related to the collision geometry. Common impact parameter filters are based upon the measured multiplicity of charged particles [14-17], the transverse energy [18], or the summed charge of particles emitted at intermediate rapidity [19]. For collisions with incident energies of a few hundred MeV per nucleon, the summed charge,  $Z_{\text{bound}}$ , of particles with atomic number  $Z \geq 2$  [20] has also been used. This quantity is the complement of the combined p, d, and t multiplicity. At lower energies,  $E/A \approx 20-50$  MeV, comparable information on impact parameter has

been extracted from measurements of the velocities of fusion-like residues [21-23], charged particle multiplicities [23,24], or neutron multiplicities [21,25].

*A priori* it is unclear to what extent the various techniques select similar or equivalent impact parameters, and whether one technique provides superior resolution as compared to another. At low energies, cross calibrations have been performed between the linear momentum transfer techniques and the emitted charged [24] or neutral particle multiplicities [21]. In this paper, we investigate  $^{36}\text{Ar}+^{197}\text{Au}$  collisions at incident energies of  $E/A=50, 80,$  and  $110$  MeV and explore the relation between impact parameter filters based upon the charged-particle multiplicity,  $N_C$ , the total transverse kinetic energy of detected charged particles,  $E_t$ , the mid-rapidity charge,  $Z_y$ , and the multiplicity of hydrogen nuclei,  $N_1$  (the complement of  $Z_{\text{bound}}$ ).

The paper is organized as follows. A brief summary of experimental details is given in Section II. In Section III, we define the various impact parameter filters. In Section IV we compare the relative scales derived from the different observables and investigate their cross-correlations. In Section V, the efficiency of the individual impact parameter filters is quantified in terms of their ability to suppress contributions from projectile fragments and fast particles emitted at forward angles. A summary and conclusions are given in Section VI. This paper is part of a systematic study of  $^{36}\text{Ar}+^{197}\text{Au}$  reactions over a broad range of incident energies performed with the MSU Miniball, a low-threshold  $4\pi$  phoswich detector [26]. A number of results, especially at lower energy, have already been published [27-30], and further work is in progress.

## II. Experimental setup

The experiment was performed with  $^{36}\text{Ar}$  beams extracted from K1200 cyclotron at the National Superconducting Cyclotron Laboratory of Michigan State University. The beam energies per nucleon were  $E/A=50, 80,$  and  $110$  MeV and the extracted intensities were typically  $10^8$  particles per second. The areal density of the gold target was approximately  $1 \text{ mg/cm}^2$ .

Light particles and complex fragments were detected with the MSU Miniball phoswich detector array [26]. In the present experiment, the array covered scattering angles of  $\Theta_{\text{lab}}=9^\circ\text{-}160^\circ$  and a solid angle corresponding to 89% of  $4\pi$ . Details about the detector geometry are given in refs. [26,29]. The detector array was actively cooled and temperature stabilized. Gain drifts of the photomultiplier tubes were monitored by a light pulser system [26]. All events in which at least two detectors fired were recorded on magnetic tape. Random coincidences were negligible due to the low beam intensity.

Each phoswich detector consisted of a  $40\mu\text{m}$  ( $4 \text{ mg/cm}^2$ ) thick plastic scintillator foil backed by a 2 cm thick CsI(Tl) crystal. All detectors had aluminized mylar foils ( $0.15 \text{ mg/cm}^2$  mylar and  $0.02 \text{ mg/cm}^2$  aluminum) placed in front of the plastic scintillator foils. As a precaution against secondary electrons, the detectors of ring 11 ( $\theta=140^\circ\text{-}160^\circ$ ) were covered by Pb-Sn foils of  $5 \text{ mg/cm}^2$  areal density. Particles punching through the  $4 \text{ mg/cm}^2$  plastic scintillator foils were identified by atomic number up to  $Z=18$ , and for H and He isotopes by mass number, as well. Approximate energy thresholds are  $E_{\text{th}}/A\approx 2$  MeV for  $Z=3$ ,  $E_{\text{th}}/A\approx 3$  MeV for  $Z=10$ , and  $E_{\text{th}}/A\approx 4$  MeV for  $Z=18$  fragments. Low-energy particles stopped in the scintillator foils were recorded but could not be identified by atomic number.

Energy calibrations of forward detectors were obtained by measuring the elastic scattering of  ${}^4\text{He}$ ,  ${}^6\text{Li}$ ,  ${}^{10}\text{B}$ ,  ${}^{12}\text{C}$ ,  ${}^{16}\text{O}$ ,  ${}^{20}\text{Ne}$  and  ${}^{35}\text{Cl}$  beams from a  ${}^{197}\text{Au}$  target at incident energies of  $E({}^4\text{He})/A = 4.5, 9.4, 12.9, 16,$  and  $20$  MeV;  $E({}^6\text{Li})/A = 8.9$  MeV;  $E({}^{10}\text{B})/A = 15$  MeV;  $E({}^{12}\text{C})/A = 6, 8, 13,$  and  $20$  MeV;  $E({}^{16}\text{O})/A = 6, 8, 16,$  and  $20$  MeV;  $E({}^{20}\text{Ne})/A = 10.6, 11.3, 13.3, 15.0,$  and  $19.8$  MeV; and  $E({}^{35}\text{Cl})/A = 8.8, 12.3,$  and  $15$  MeV. For detectors in rings 1-4, these calibrations are estimated to be accurate within 5%. Calibrations of more backward detectors were obtained from the energies of light-particles punching through the CsI(Tl) crystals and from extrapolations of the average response of detectors at more forwards angles. The resulting uncertainties in energy calibration at more backward angles are considerably larger, typically of the order of 10% and for some detectors as large as 20%.

### III. Definition of impact parameter filters

In this paper, we will use the following quantities to extract information on the magnitude of the impact parameter:

(1) The charged particle multiplicity,  $N_C$ . This quantity includes all charged particles detected by the Miniball, even if they are not identified (as, for example, heavy fragments stopped in the scintillator foils). Multiple hits in a single detector module are counted as single hits, even if they can be clearly identified as double hits (as is generally the case for double hits by  $\alpha$ -particles). The number  $N_C$  is therefore equal to the number of detectors in which at least one charged particle is detected in a given event.

(2) The total transverse kinetic energy of identified particles,  $E_t$ , is defined [29] as

$$E_t = \sum_i E_i \sin^2 \theta_i = \sum_i (p_i \sin \theta_i)^2 / 2m_i . \quad (1)$$

Here,  $E_i$ ,  $p_i$ , and  $\theta_i$  denote the kinetic energy, momentum and emission angle of particle  $i$  with respect to the beam axis.

(3) The mid-rapidity charge,  $Z_y$ , is defined [19] as the summed charge of all identified particles of rapidity  $y$  with

$$0.25y_{\text{c.m.}} \leq y \leq 0.75y_{\text{proj.}} + 0.25y_{\text{c.m.}} \quad (2a)$$

or, equivalently,

$$0.75y'_{\text{targ.}} \leq y' \leq 0.75y'_{\text{proj.}} . \quad (2b)$$

Here, primed quantities are defined in the center-of-mass rest frame of the total system and unprimed quantities are defined in the laboratory frame of reference;  $y_{\text{c.m.}}$ ,  $y_{\text{targ.}}$  and  $y_{\text{proj.}}$  denote the rapidities of the total center-of-mass system and of target and projectile, respectively. The rapidity,  $y$ , of a particle is defined [31] as

$$y = \frac{1}{2} \ln \left\{ \frac{\sqrt{m^2 + p^2} + p \cos \theta}{\sqrt{m^2 + p^2} - p \cos \theta} \right\} = \tanh^{-1}(\beta \cos \theta) , \quad (3)$$

where  $m$ ,  $\beta$ , and  $p$  denote the particle's mass, velocity and momentum, respectively.

(4) The identified hydrogen multiplicity,  $N_1$ . This quantity is defined as the number of detectors in which a  $Z=1$  particle is identified. The definition includes hydrogen nuclei which punch through the CsI(Tl) crystals and double

hits by p, d, or t.  $N_1$  is the complement of  $Z_{\text{bound}}$  [20], the summed charge of particles with atomic number of  $Z \geq 2$ .

Figures 1-3 show the measured correlations between the quantities  $N_C$ ,  $E_t$ ,  $Z_y$ , and  $N_1$ . At all incident energies, the four quantities are strongly correlated. In general, an increase in the value of one observable is accompanied by an increase in the value of the other three observables. From this observation one may already conclude that all four quantities are suitable for impact parameter selection - or none. However, the correlation between  $E_t$  and  $N_C$  gives evidence for a slight saturation of  $N_C$  at high  $E_t$ , indicating that the transverse energy might provide a better central collision trigger than the charged particle multiplicity.

In order to construct an approximate scale for the impact parameter, we adopt the geometrical prescription of ref. [17]. For each of the quantities  $N_C$ ,  $E_t$ ,  $Z_y$ , and  $N_1$ , we assume a monotonic relationship to the impact parameter and define the reduced impact parameter scale via

$$b(X)/b_{\text{max}} = \hat{b}(X) = \left\{ \int_X^{\infty} \frac{dP(X')}{dX'} dX' \right\}^{1/2}, \quad (4)$$

where  $X = N_C$ ,  $E_t$ ,  $Z_y$ , and  $N_1$ ;  $dP(X)/dX$  is the normalized probability distribution for the measured quantity  $X$ , and  $b_{\text{max}}$  is the maximum impact parameter for which particles were detected in the Miniball ( $N_C \geq 2$ ). In the following, we will use the reduced impact parameter scale  $\hat{b}$  which ranges from  $\hat{b}=1$  for glancing collisions to  $\hat{b}=0$  for head-on collisions.

The quantitative relation between the reduced impact parameters  $\hat{b}(X)$  and the measured observables  $X$  ( $X = N_C$ ,  $E_t$ ,  $Z_y$ , and  $N_1$ ) is shown in Fig. 4.



Individual panels present the relationships between the reduced impact parameters  $\hat{b}(X)$  and the observables  $X=N_C, E_t, Z_y,$  and  $N_1$  shown on the abscissae, and the different curves show the relationships extracted for the three different incident energies.

While geometrical prescriptions implicit in Eq. 4 may provide reasonable scales for the average relation between charged-particle multiplicity and impact parameter, it is not clear, *a priori*, whether the scales extracted from the various quantities are commensurate. Furthermore, for collisions at fixed impact parameter, these quantities exhibit fluctuations of unknown magnitude. Therefore, reaction filters constructed from the various observables could have different resolution. This question will be addressed in the next sections.

#### IV. Comparison of relative scales

In order to investigate the relation between impact parameter scales extracted via Eq. 4 from the various measured observables, we have set narrow gates on impact parameters  $\hat{b}(X)$ , defined by means of an observable  $X$ , and determined the conditional distributions of impact parameters  $\hat{b}(Y)$ , constructed from different observables  $Y$  ( $Y \neq X$  and  $X, Y = N_C, E_t, Z_y, N_1$ ).

Conditional impact parameter distributions are presented in Figs. 5-8. Individual panels of these figures show conditional impact parameter distributions  $\hat{b}(Y)$  determined from the indicated observables  $Y$ . Left and right hand panels show distributions extracted for the cuts  $\hat{b}(X)=0.05-0.1$  and  $\hat{b}(X)=0.35-0.45$ , respectively. Dashed and dotted curves show results obtained by cuts placed on one observable, and solid curves show results obtained by simultaneous cuts placed on two observables. The observables  $X$  used for these cuts are indicated in the individual left-hand panels; the conventions for left and

right panels are identical. For better comparison, all conditional impact parameter distributions are normalized to unit area.

For the present reaction, impact parameter filters based upon  $N_1$  (the complement of  $Z_{\text{bound}}$ ) are considerably less selective than reaction filters based upon  $N_C$ ,  $E_t$ , and  $Z_y$ . This effect is clear from Fig. 5, which compares conditional distributions based upon  $N_1$ ,  $E_t$ , and  $Z_y$  for collisions at  $E/A=110$  MeV. The reduced resolution of impact parameter filters based upon  $N_1$  is most likely of statistical origin. For collisions at fixed impact parameter, the relative magnitude of statistical fluctuations is enhanced for the observable  $N_1$  because it contains, by definition, only a small subset of the emitted particles.

Figures 6, 7, and 8 present conditional impact parameter distributions at different energies. In general, the conditional impact parameter distributions become narrower with increasing particle energy. Qualitatively, this can be understood in terms of statistical fluctuations: at fixed impact parameter, statistical fluctuations lead to distributions in  $X=N_C$ ,  $E_t$ , and  $Z_y$  of finite widths  $\Delta X$ . For collisions at fixed impact parameter, the mean values of all quantities ( $X=N_C$ ,  $E_t$ , and  $Z_y$ ) increase with increasing projectile energy and the relative fluctuations,  $\Delta X/X$ , decrease. Hence, impact parameter determinations should become more accurate at higher energies.

At a given incident energy, rather similar conditional impact parameter distributions are extracted from different observables, with little sensitivity to the applied cut on other observables. While some differences exist, they are generally small.

Cuts on small impact parameters,  $\hat{b}(X)=0.05-0.1$ , generally produce conditional distributions,  $\hat{b}(Y)$ , peaked at larger impact parameters,  $\hat{b}(Y)\approx 0.2$ . Conditional impact parameter distributions  $\hat{b}(Y)$ , extracted for simultaneous cuts on small impact parameters,  $\hat{b}(X_1)=\hat{b}(X_2)=0.05-0.1$ , are slightly narrower and they peak at lower impact parameters,  $\hat{b}(Y)\approx 0.12-0.16$ , than those obtained from cuts on a single observable. Hence, somewhat improved selection of central collisions can be obtained from multi-dimensional cuts.

One-dimensional cuts on  $\hat{b}(E_t)=0.05-0.1$  produce narrower distributions in  $\hat{b}(N_C)$  and  $\hat{b}(Z_y)$  than the alternative one-dimensional cuts on  $\hat{b}(Z_y)$  and  $\hat{b}(N_C)$ , respectively. Furthermore, two-dimensional cuts on small impact parameters produce narrower distributions for  $\hat{b}(E_t)$  than for  $\hat{b}(N_C)$  and  $\hat{b}(Z_y)$ . These observations suggest that filters based upon  $E_t$  may more effective in selecting central collisions than filters based upon the other observables investigated in this paper.

For cuts on intermediate impact parameters,  $\hat{b}(X)=0.35-0.45$ , the conditional distributions  $\hat{b}(Y)$  are peaked at values close to  $\hat{b}(Y)\approx 0.4$ , i.e. close to the cut on  $\hat{b}(X)$ . This correspondence between the impact parameter scales derived from different observables improves at higher beam energies, indicating that all impact parameter filters have improved resolution at higher energies. Again, small improvements in resolution are obtained by the application of two-dimensional cuts. However, these improvements are less pronounced than that seen for very small impact parameters.

The similarities of the various conditional impact parameter distributions shown in Figs. 6-8 indicate that the three observables ( $N_C$ ,  $E_t$ , and  $Z_y$ ) have

similar selectivity on impact parameter. Figure 9 summarizes and corroborates these findings in a compact form. The individual panels of the figure show the centroids (points) and widths at half maximum (vertical bars) of conditional impact parameter distributions selected by narrow cuts on impact parameters, centered at  $\hat{b}(X)=0.1, \dots, 0.9$  and extracted from other observables  $X$ . Left, center and right columns show data at  $E/A=50, 80,$  and  $110$  MeV, respectively. Overall, the relation between the individual impact parameter scales is fairly linear with significant deviations occurring only for small and large impact parameters. Such deviations must be expected at the edges of the impact parameter scales whenever the two-dimensional correlations shown in Figs. 1-3 have finite widths and some curvature.

Furthermore, the widths of the various conditional distributions are rather similar. Some modest improvement in impact parameter selection can be obtained by using multi-dimensional cuts (solid circular points). These improvements are difficult to quantify since none of the conditional distributions can be narrower than their natural widths at a given sharp impact parameter. Since the widths from one- and two-dimensional cuts are rather similar, one may surmise that the widths extracted from the two-dimensional cuts are close to the intrinsic resolution of the respective impact parameter filters.

Improved impact parameter selection could be expected from observables (or combinations of observables) which are less subject to statistical fluctuations. For example, one may argue that central collisions could be reconstructed by an accurate determination of the energy deposited into internal degrees of freedom. For fixed excitation energy, the number of emitted

charged particles will exhibit considerable fluctuations due to statistical partitions of the de-excitation energy among neutrons, protons and complex particles, all of which are emitted over a broad energy spectrum. Improved reconstructions of the initial excitation energy could be expected from simultaneous measurements of neutral and charged particle multiplicities, but some fluctuations would remain due to the finite energy distributions of the emitted particles (and varying separation energies). One should expect that statistical fluctuations may be smaller for the total transverse energy of the emitted charged particles since this quantity suffers only from the random partition of the excitation energy into charged and neutral particles and into longitudinal and transverse velocities. Close inspection of Figs. 5-8 reveals that the double-gated  $\hat{b}(E_t)$  distributions are slightly narrower than the other impact parameter distributions, possibly indicating that the transverse energy exhibits a particularly good selectivity for central collisions.

At higher energies and for noncentral collisions, geometric considerations may lead to the expectation that the intermediate rapidity charge might become competitive or even more appropriate since it could provide a better measure of the participant zone. Unfortunately, microscopic reaction models do not yet describe realistic descriptions of complex particle emission processes, and fluctuations in  $Z_y$  due to fragment formation at the interfaces of the participant and spectator zones are difficult to assess. Since a substantial portion of the emitted nuclear matter emerges in the form of bound clusters, it is not clear which observables (or combinations of observables) provide optimal impact parameter selectivity. In the next section, we explore this question further by investigating an alternative measure for the selectivity of various impact parameter filters which is based upon their ability to suppress the emission of fast fragments at forward angles.

## V. Suppression of projectile-like fragments

In this section, we explore the efficiency of various impact parameter filters in terms of their ability to suppress projectile-like fragments emitted with near-beam velocity at forward angles.

For illustration, Figs. 10-12 show the energy spectra of beryllium (left-hand panels) and carbon (right-hand panels) nuclei detected in Rings 1-10 in the Miniball for incident energies of  $E/A=50, 80,$  and  $110$  MeV, respectively. Top and bottom panels show the energy spectra gated by cuts on the charged particle multiplicity corresponding to  $\hat{b}(N_C) \gtrsim 0.6$  and  $\hat{b}(N_C) \lesssim 0.3$ , respectively. At all incident energies, the energy spectra gated by large impact parameters exhibit pronounced maxima at forward angles which correspond to fragment velocities close to the beam velocity. Such projectile-like contributions are strongly suppressed in the energy spectra selected by high-multiplicity cuts corresponding to  $\hat{b}(N_C) \lesssim 0.3$ , as qualitatively expected from simple geometrical considerations within the framework of a participant-spectator approximation. These qualitative findings are consistent with observations at lower energy,  $E/A=35$  MeV [30]. They indicate that impact parameter filters based upon charged particle multiplicity are rather effective in selecting collisions with large geometrical overlap between target and projectile even in situations where simple participant-spectator models are not expected to be accurate in detail.

In order to provide a more quantitative basis for discussing the effects of impact parameter filtering on the measured energy spectra, we fit the energy spectra with a simple three-source parameterization corresponding to the superposition of three Maxwellian distributions centered at velocities  $v_i$  and characterized by temperature parameters  $T_i$ :

$$\frac{d^2P}{dEd\Omega} = \sum_{i=1}^3 \sigma_i(E, \theta) = \sum_{i=1}^3 N_i \sqrt{E-V_C} \exp\{-(E-V_C+E_i-2\sqrt{E_i(E-V_C)} \cos\theta)/T_i\}, (5)$$

where

$$E_i = \frac{1}{2} m v_i^2 \quad (6)$$

is the energy of a particle at rest in source  $i$ . The parameter  $V_C$  is introduced to roughly account for Coulomb repulsion from a heavy charge assumed, for simplicity, at rest in the laboratory system [22,32]. Fits obtained with this parametrization are shown as solid curves in Figs. 10-12. The corresponding parameters are listed in Table 1.

A word of caution is necessary. Since our energy calibrations at backward angles have considerable uncertainties, the source parameters listed in Table 1 may have large systematic uncertainties. In particular, the parameters of the slow target-like sources ( $i=3$ ) must be viewed with caution, and the temperature parameters  $T_3$  should not be misconstrued as accurate temperature measurements for target-like residues.

Nevertheless, the fits allow estimates of the relative contributions from fast projectile-like sources and intermediate-velocity "nonequilibrium" sources. At all energies, peripheral collisions ( $\hat{b} \gtrsim 0.6$ ) are characterized by strong contributions from projectile-like sources. Such contributions are strongly suppressed for more "central" collisions ( $\hat{b} \lesssim 0.3$ ). However, central collisions have significant contributions from intermediate-velocity "nonequilibrium" sources representing emission during the early, nonequilibrated stages of the reaction. Our present findings are consistent with previous observations at lower energy [30]. Clearly, accurate descriptions of energy spectra and angular distributions

will require theoretical treatments which allow the incorporation of emission from the earlier non-equilibrated phases of the reaction, as well as from the later more equilibrated stages.

In order to provide a more quantitative measure of the selectivity of the impact parameter filter based upon the charged particle multiplicity, we have fitted the multiplicity selected energy spectra of representative complex particles (He, Li, Be, C) with Eqs. 5-6 and determined the relative contribution,  $\sigma_{\text{proj}}/\sigma_{\text{tot}}$ , of the projectile-like source to the total particle yield. This contribution was evaluated by integrating the respective sources over all angles and energies:

$$\sigma_{\text{proj}} = \iint \sigma_1(E, \theta) dE d\Omega, \quad (7)$$

$$\sigma_{\text{tot}} = \sum_{i=1}^3 \iint \sigma_i(E, \theta) dE d\Omega, \quad (8)$$

We refrained from analyzing the energy spectra of hydrogen nuclei, because of the restricted dynamic range of the Miniball. Moreover, light particles (especially nucleons) are less suitable for such an analysis, because of their comparatively large mean free path and because of the fact that "thermal" smearing of the energy spectra is more serious for light particles than for intermediate mass fragments. As a consequence, collective source velocity components are more difficult to unravel from the energy spectra of light particles.

Figure 13 shows ratios  $\sigma_{\text{proj}}/\sigma_{\text{tot}}$  extracted from the energy spectra of He, Li, Be and C nuclei selected by different cuts on charged particle multiplicity for the  $^{36}\text{Ar} + ^{197}\text{Au}$  reactions at  $E/A=110$  MeV. For illustration, a scale of the



reduced impact parameter  $\hat{b}(N_C)$  and a pictorial illustration of the geometric overlap between projectile and target nuclei are included in the figure. While such a simplistic graphic visualization must not be taken too seriously, it nevertheless illustrates that complete overlap between projectile and target nuclei is only achieved for relatively small impact parameters, representing less than 10% of the total reaction cross section. Even in such a naive geometrical picture, some emission from projectile-like sources must be expected down to impact parameters of  $\hat{b} \sim 0.4$ . These simple expectations are fulfilled rather nicely for the emission of intermediate mass fragments for which projectile-like contributions are strongly suppressed at large multiplicities (small impact parameters). The suppression of projectile-like contributions is more effective for heavier (e.g. carbon nuclei) than for lighter particles (e.g.  $\alpha$ -particles). In fact, the emission of fast  $\alpha$ -particles does not follow the simple trends expected from simple geometrical arguments. Possibly  $\alpha$ -particle emission already sets in at the early contact phase of the reaction and can, therefore, not be described by a simple participant-spectator picture.

In order to compare of the effects of different impact parameter filters on the shapes of the energy spectra at forward angles, we have analyzed the energy spectra of particles detected in rings 1 and 2 ( $\theta=9^\circ$ - $23^\circ$ ) and determined the "fast-particle fraction",  $\sigma(v > \frac{1}{2}v_p) / \sigma_{tot}$ , defined as the fraction of particles detected in rings 1 and 2 with velocities larger than half the projectile velocity. This simple quantity provides qualitatively similar insight as the quantity  $\sigma_{proj} / \sigma_{tot}$  obtained from the moving source decomposition, but without necessitating cumbersome multi-parameter fits with Eq. 5. The fast-particle fraction is well defined and it can be established with good statistical accuracy even for narrow cuts on impact parameter. Furthermore, this quantity is insensitive to

source-parameter ambiguities associated with fits to energy spectra which have poor statistical accuracy due to narrow cuts on impact parameter.

Fast-particle fractions extracted for various cuts on impact parameter are shown Figs. 14-16. Different figures show results for the three incident energies. Individual panels show the fast-particle fractions for He, Li, Be and C nuclei, and different symbols depict results obtained by different impact parameter filters.

At all energies, the fast-particle fractions are monotonic functions of the reduced impact parameter. The suppression of fast particles for cuts on small impact parameters is particularly effective for beryllium and carbon nuclei. The suppression of fast particles is less effective for  $\alpha$ -particles. These qualitative observations are consistent with the results obtained with the moving source decomposition shown in Fig. 13. For impact parameters  $\hat{b} \lesssim 0.6$ , all three impact parameter filters produce rather consistent fast-particle fractions. For intermediate and small impact parameters ( $\hat{b} \lesssim 0.6$ ), filters constructed from  $N_C$ ,  $E_t$ , and  $Z_y$  appear to provide comparable resolution. Slightly better suppressions of the fast-particle fractions can be obtained by employing triple cuts on values of the impact parameters reconstructed from  $N_C$ ,  $E_t$ , and  $Z_y$  (see star-shaped points). Consistent with our previous findings, these improvements are relatively inconspicuous.

For larger impact parameters, however, the differences between the various techniques become more significant, particularly at the higher energies. Such differences may be caused by statistical fluctuations of the quantities  $N_C$ ,  $E_t$ , and  $Z_y$ . The relative magnitude of these fluctuations should be largest for peripheral collisions which are characterized by small mean

values  $\langle N_C \rangle$ ,  $\langle E_t \rangle$ , and  $\langle Z_y \rangle$ . As a consequence, selections of large impact parameters may be associated with larger uncertainties than selections of smaller impact parameters.

## VI. Summary and conclusion

In this paper, we explored the selection of impact parameters via impact parameter filters based upon the detected charged particle multiplicity  $N_C$ , the transverse energy  $E_t$ , the intermediate rapidity charge  $Z_y$ , and the identified hydrogen multiplicity  $N_1$  (which is the complement of  $Z_{\text{bound}}$ , the summed charge of clusters with  $Z \geq 2$  [20]). For the reactions studied in this paper, all of these quantities were shown to be correlated with each other and all display some sensitivity to the impact parameter. By applying a simple geometric prescription for the construction of a reduced impact parameter scale, quantitative comparisons of the various impact parameter scales were performed.

Average impact parameters deduced from these quantities were found to be mutually consistent, with small deviations occurring at the boundaries of the reduced impact parameter scale,  $\hat{b}=0$  and  $\hat{b}=1$ . In order to assess the relative resolutions of the various impact parameter filters, we explored distributions of impact parameters  $\hat{b}(Y)$  for events selected by narrow cuts on alternative impact parameter scales  $\hat{b}(X)$ , where  $X, Y = N_C, E_t, Z_y$ , and  $N_1$ . As an alternative measure, we compared the suppression of fast fragments emitted at forward angles by corresponding cuts on  $\hat{b}(N_C)$ ,  $\hat{b}(E_t)$ , and  $\hat{b}(Z_y)$ .

Based upon these criteria, impact parameter selections derived from the total charged particle multiplicity  $N_C$ , the transverse energy  $E_t$  and the intermediate rapidity charge  $Z_y$  were found to be very similar, with some differences occurring at large impact parameters where fluctuations appear to become a

limiting factor. Somewhat worse resolution was obtained by employing the hydrogen multiplicity  $N_1$  (the complement of  $Z_{\text{bound}}$ ). This effect is related to the fact that  $N_1 \leq N_C$  and, hence,  $\Delta N_1/N_1 \geq \Delta N_C/N_C$ . For a given impact parameter, the larger fractional fluctuations of  $\Delta N_1/N_1$  therefore lead to larger fluctuations  $\Delta \hat{b}(N_1)/\hat{b}(N_1)$  in the deduced impact parameter.

Slightly improved selection of central collisions can be obtained by the use of multi-dimensional gates placed on different observables. In this regard, the future use of instruments capable of detecting neutral and charged particle observables in  $4\pi$  geometry appears particularly promising.

This work is based upon work supported by the National Science Foundation under Grant numbers PHY-86-11210, PHY-89-13815. WGL acknowledges the receipt a of U.S. Presidential Young Investigator Award.

## References

- † Present address: Lawrence Berkeley Laboratory, Berkeley, CA 94720, USA
- \* Present address: Indiana University Cyclotron Facility, Indiana University, Bloomington, IN 47405
1. G. Sayer, H., Chandra, and U. Mosel, U. Nucl. Phys. A, 24, 221 (1976).
  2. H.R. Jaqaman, A.Z. Mekjian, and L. Zamick, Phys. Rev. C27, 2782 (1983);  
H.R. Jaqaman, A.Z. Mekjian, and L. Zamick, Phys. Rev. C29, 2067 (1984).
  3. M.W. Curtin, H. Toki, and D.K. Scott, Phys. Lett. B 123, 289 (1983).
  4. J.H. Rose, J.P. Vary, and J.R. Smith, Phys. Rev. Lett. 53, 344 (1984).
  5. J.C. Collins and M.J. Perry, Phys. Rev. Lett. 34, 1353 (1975).
  6. P.D. Morley and M.B. Kislinger, Phys. Rep. 51, 63 (1979) and references therein.
  7. E.Shuryak, Phys. Rep. 61, 71 (1980) and references therein.
  8. L.D. McLerran and B. Svetitsky, Phys. Lett. B 98, 195 (1981).
  9. J. Kuti, J. Polònyi and K. Szlachányi, Phys. Lett. B 98, 199 (1981).
  10. K. Sneppen and L. Vinet, Nucl. Phys. A480, 342 (1988).
  11. T.J. Schlagel, and V.R. Pandharipande, Phys. Rev. C36, 162 (1987).
  12. L.P. Csernai, and J.I. Kapusta, Phys. Rep. 131, 233 (1986), and references contained therein.
  13. W.G. Lynch, Ann. Rev. Nucl. Part. Sci. 37, 493 (1987), and references contained therein.
  14. M.B. Tsang, G.F. Bertsch, W.G. Lynch, and M. Tohyama, Phys. Rev. C40, 1685 (1989).
  15. R. Stock, Phys. Reports. 135, (1986) 259.
  16. H. Stöcker and W. Greiner, Phys. Reports 137, 277 (1986).
  17. C. Cavata, M. Demoulin, J. Gosset, M.C. Lemaire, D. L'Hôte, J. Poitou, and O. Valette, Phys. Rev. C42, 1760 (1990).

18. H.G. Ritter, Nucl. Phys. A488, 651c (1988).
19. C.A. Ogilvie, D. Cebra, J. Clayton, S. Howden, J. Karn, A. Vander Molen, G.D. Westfall, W.K. Wilson, and J.S. Winfield, Phys. Rev. C40, 654 (1989).
20. J. Hubele, P. Kreutz, J.C. Adloff, M. Begemann-Blaich, P. Bouissou, G. Imme, I. Iori, G.J. Kunde, S. Leray, V. Lindenstruth, Z. Liu, U. Lynen, R.J. Meijer, U. Milkau, A. Moroni, W.F.J. Müller, C. Ngô, C.A. Ogilvie, J. Pochodzalla, G. Raciti, G. Rudolf, H. Sann, A. Schüttauf, W. Seidel, L. Stuttge, W. Trautmann, and A. Tucholski, Z. Phys. A340, 263 (1991).
21. J. Galin, Nucl. Phys. A447, 519c (1985).
22. T.C. Awes, G. Poggi, C.K. Gelbke, B.B. Back, B.G. Glagola, and V.E. Viola, Jr., Phys. Rev. C24, 89, (1981).
23. Z. Chen, C.K. Gelbke, J. Pochodzalla, C.B. Chitwood, D.J. Fields, W.G. Gong, W.G. Lynch, and M.B. Tsang, Nucl. Phys. A473, 564 (1987).
24. M.B. Tsang, Y.D. Kim, N. Carlin, Z. Chen, R. Fox, C.K. Gelbke, W.G. Gong, W.G. Lynch, T. Murakami, T.K. Nayak, R.M. Ronningen, H.M. Xu, F. Zhu, L. Sobotka, D. Stracener, D.G. Sarantites, Z. Majka, V. Abenante, and H. Griffin, Phys. Lett. B220, 492 (1989).
25. M. Morjean, et al., Phys. Lett. B203, 215 (1988).
26. R.T. de Souza, N. Carlin, Y.D. Kim, J. Ottarson, L. Phair, D.R. Bowman, C.K. Gelbke, W.G. Gong, W.G. Lynch, R.A. Pelak, T. Peterson, G. Poggi, M.B. Tsang, and H.M. Xu, Nucl. Instr. and Meth. A295, 109 (1990).
27. Y.D. Kim, R.T. de Souza, D.R. Bowman, N. Carlin, C.K. Gelbke, W.G. Gong, W.G. Lynch, L. Phair, M.B. Tsang, F. Zhu, and S. Pratt, Phys. Rev. Lett. 67, 14 (1991).
28. R.T. de Souza, L. Phair, D.R. Bowman, N. Carlin, C.K. Gelbke, W.G. Gong, Y.D. Kim, M.A. Lisa, W.G. Lynch, G.F. Peaslee, M.B. Tsang, H.M. Xu, F. Zhu, and W.A. Friedman, Phys. Lett. B268, 6 (1991).

29. M.B. Tsang, R.T. de Souza, Y.D. Kim, D.R. Bowman, N. Carlin, C.K. Gelbke, W.G. Gong, W.G. Lynch, L. Phair, and F. Zhu, Phys. Rev. C44, 2065 (1991).
30. Y.D. Kim, R.T. de Souza, D.R. Bowman, N. Carlin, C.K. Gelbke, W.G. Gong, W.G. Lynch, L. Phair, M.B. Tsang, and F. Zhu, Phys. Rev. C45, 338 (1992).
31. A.S. Goldhaber and H.H. Heckman, Ann. Rev. Nucl. Part. Sci. 28, 161 (1978).
32. C.B. Chitwood, D.J. Fields, C.K. Gelbke, D.R. Klesch, W.G. Lynch, M.B. Tsang, T.C. Awes, R.L. Ferguson, F.E. Obenshain, F. Plasil, R.L. Robinson, and G.R. Young, Phys. Rev. C34, 858 (1986).
33. P. Beckmann, et al., Mod. Phys. Lett. A2, 163 (1987).

Table 1

Moving source parameters used to fit the energy spectra in Figs. 10-12. For beryllium and carbon nuclei, the Coulomb parameters were  $V_C=32.9$  and  $47.2$  MeV, respectively. The normalization constants  $N_i$  are given in units of  $[10^{-6}/(\text{sr}\cdot\text{MeV}^{3/2})]$ ; units for  $E/A$  and  $T_i$  are in [MeV]. (At the energies  $E/A=50, 80, 110$  MeV, the velocities of the projectile are:  $\beta_{\text{proj}}=0.32, 0.39,$  and  $0.45$ ; the velocities of the total center-of-mass system are:  $\beta_{\text{cm}}=0.051, 0.065,$  and  $0.077,$  respectively.)

$E/A$	$Z$	$N_C$	$N_1$	$\beta_1$	$T_1$	$N_2$	$\beta_2$	$T_2$	$N_3$	$\beta_3$	$T_3$
50	4	2-13	106	0.273	9.2	40.2	0.180	17.0	55.2	0.079	12.6
50	6	2-13	179	0.275	9.7	23.1	0.177	17.4	39.6	0.071	13.1
50	4	$\geq 19$	51	0.186	14.5	231	0.098	14.3	171	0.036	8.6
50	6	$\geq 19$	2.07	0.221	16.3	69.3	0.141	13.9	211	0.067	13.6
80	4	2-16	107	0.303	11.1	16.3	0.190	20.2	44.1	0.073	12.9
80	6	2-16	53.7	0.313	12.5	5.46	0.169	20.0	34.6	0.066	12.4
80	4	$\geq 25$	28.1	0.218	21.8	152	0.106	21.9	212	0.046	12.0
80	6	$\geq 25$	1.08	0.257	23.5	31.5	0.142	23.7	238	0.071	16.9
110	4	2-18	26.1	0.326	17.5	6.88	0.165	23.3	34.6	0.060	12.6
110	6	2-18	4.37	0.333	19.4	1.67	0.155	22.3	25.4	0.057	12.4
110	4	$\geq 30$	9.48	0.248	31.9	91.8	0.123	29.9	251	0.055	15.8
110	6	$\geq 30$	12.1	0.406	23.3	17.4	0.142	33.8	218	0.068	19.4



## Figure Captions

**Fig. 1:** Correlations between charged particle multiplicity  $N_C$ , transverse energy  $E_t$ , intermediate rapidity charge  $Z_y$ , and identified hydrogen multiplicity  $N_1$  observed for  $^{36}\text{Ar}+^{197}\text{Au}$  collisions at  $E/A=50$  MeV. Adjacent contours of different color differ by factors of 5.

**Fig. 2:** Correlations between charged particle multiplicity  $N_C$ , transverse energy  $E_t$ , intermediate rapidity charge  $Z_y$ , and identified hydrogen multiplicity  $N_1$  observed for  $^{36}\text{Ar}+^{197}\text{Au}$  collisions at  $E/A=80$  MeV. Adjacent contours of different color differ by factors of 5.

**Fig. 3:** Correlations between charged particle multiplicity  $N_C$ , transverse energy  $E_t$ , intermediate rapidity charge  $Z_y$ , and identified hydrogen multiplicity  $N_1$  observed for  $^{36}\text{Ar}+^{197}\text{Au}$  collisions at  $E/A=110$  MeV. Adjacent contours of different color differ by factors of 5.

**Fig. 4:** Reduced impact parameter scales  $\hat{b}(X)$  extracted from the measured quantities  $X=N_C$ ,  $E_t$ ,  $Z_y$ , and  $N_1$ . Each panel show the relation extracted for the indicated observable; different curves represent the relations extracted at the three incident energies.

**Fig. 5:** Conditional impact parameter distributions  $\hat{b}(Y)$  extracted for  $Y=Z$  (top panels),  $Y=N_1$  (center panels), and  $Y=E_t$  (bottom panels) for the  $^{36}\text{Ar}+^{197}\text{Au}$  reaction at  $E/A=110$  MeV. Left and right hand panels show distributions selected by impact parameter cuts  $\hat{b}(X)=0.05-0.1$  and  $\hat{b}(X)=0.35-0.45$  on the indicated observables ( $X=N_1$ ,  $E_t$ , and  $Z_y$ ). All impact parameter scales were constructed according to Eq. 4.

**Fig. 6:** Conditional impact parameter distributions  $\hat{b}(Y)$  extracted for  $Y=Z$  (top panels),  $Y=N_C$  (center panels), and  $Y=E_t$  (bottom panels) for the  $^{36}\text{Ar}+^{197}\text{Au}$  reaction at  $E/A=50$  MeV. Left and right hand panels show distributions selected by impact parameter cuts  $\hat{b}(X)=0.05-0.1$  and  $\hat{b}(X)=0.35-0.45$  on the indicated observables ( $X=N_C$ ,  $E_t$ , and  $Z_y$ ). All impact parameter scales were constructed according to Eq. 4.

**Fig. 7:** Conditional impact parameter distributions  $\hat{b}(Y)$  extracted for  $Y=Z$  (top panels),  $Y=N_C$  (center panels), and  $Y=E_t$  (bottom panels) for the  $^{36}\text{Ar}+^{197}\text{Au}$  reaction at  $E/A=80$  MeV. Left and right hand panels show distributions selected by impact parameter cuts  $\hat{b}(X)=0.05-0.1$  and  $\hat{b}(X)=0.35-0.45$  on the indicated observables ( $X=N_C$ ,  $E_t$ , and  $Z_y$ ). All impact parameter scales were constructed according to Eq. 4.

**Fig. 8:** Conditional impact parameter distributions  $\hat{b}(Y)$  extracted for  $Y=Z$  (top panels),  $Y=N_C$  (center panels), and  $Y=E_t$  (bottom panels) for the  $^{36}\text{Ar}+^{197}\text{Au}$  reaction at  $E/A=110$  MeV. Left and right hand panels show distributions selected by impact parameter cuts  $\hat{b}(X)=0.05-0.1$  and  $\hat{b}(X)=0.35-0.45$  on the indicated observables ( $X=N_C$ ,  $E_t$ , and  $Z_y$ ). All impact parameter scales were constructed according to Eq. 4.

**Fig. 9:** Centroids and widths at half maximum of conditional impact parameter distributions selected by cuts on impact parameters constructed from other observables  $X$  indicated in the individual panels. For ease of presentation, the open points have been displaced from the centers of the gates on  $\hat{b}(X)$ . Top, center and bottom panels show the values for impact parameter scales constructed from  $N_C$ ,  $E_t$ , and  $Z_y$ , respectively. Left, center and right hand columns show data for the  $^{36}\text{Ar}+^{197}\text{Au}$  reaction at  $E/A=50$ , 80, and 110 MeV.

**Fig.10:** Energy spectra of beryllium (left hand panels) and carbon (right hand panels) nuclei emitted in peripheral ( $\hat{b} \gtrsim 0.6$ , top panels) and central ( $\hat{b} \lesssim 0.3$ ; bottom panels)  $^{36}\text{Ar} + ^{197}\text{Au}$  collisions at  $E/A=50$  MeV. The exact cuts on the measured charged particle multiplicity are given in the figure. The solid curves are fits with Eq. 5; the parameters are listed in Table 1.

**Fig.11:** Energy spectra of beryllium (left hand panels) and carbon (right hand panels) nuclei emitted in peripheral ( $\hat{b} \gtrsim 0.6$ , top panels) and central ( $\hat{b} \lesssim 0.3$ ; bottom panels)  $^{36}\text{Ar} + ^{197}\text{Au}$  collisions at  $E/A=80$  MeV. The exact cuts on the measured charged particle multiplicity are given in the figure. The solid curves are fits with Eq. 5; the parameters are listed in Table 1.

**Fig.12:** Energy spectra of beryllium (left hand panels) and carbon (right hand panels) nuclei emitted in peripheral ( $\hat{b} \gtrsim 0.6$ , top panels) and central ( $\hat{b} \lesssim 0.3$ ; bottom panels)  $^{36}\text{Ar} + ^{197}\text{Au}$  collisions at  $E/A=110$  MeV. The exact cuts on the measured charged particle multiplicity are given in the figure. The solid curves are fits with Eq. 5; the parameters are listed in Table 1.

**Fig.13:** Relative contribution of projectile-like source extracted from the energy spectra of He, Li, Be and C nuclei selected by different cuts on charged particle multiplicity for  $^{36}\text{Ar} + ^{197}\text{Au}$  collisions at  $E/A=110$  MeV. A scale of the reduced impact parameter  $\hat{b}(N_C)$  and a pictorial illustration of the geometric overlap between projectile and target nuclei are included.

**Fig.14:** Fast-particle fractions (fraction of particles detected at  $\theta=9^\circ-23^\circ$  with velocities greater than half the beam velocity) for  $^{36}\text{Ar} + ^{197}\text{Au}$  collisions at  $E/A=50$  MeV. Solid points, open squares and open circles depict values determined for narrow cuts on the reduced impact parameters determined from  $N_C$ ,

$E_t$ , and  $Z_y$ ; star-shaped points represent simultaneous cuts on  $\hat{b}(N_C)$ ,  $\hat{b}(E_t)$ , and  $\hat{b}(Z_y)$ .

**Fig.15:** Fast-particle fractions (fraction of particles detected at  $\theta=9^\circ-23^\circ$  with velocities greater than half the beam velocity) for  $^{36}\text{Ar}+^{197}\text{Au}$  collisions at  $E/A=80$  MeV. Solid points, open squares and open circles depict values determined for narrow cuts on the reduced impact parameters determined from  $N_C$ ,  $E_t$ , and  $Z_y$ ; star-shaped points represent simultaneous cuts on  $\hat{b}(N_C)$ ,  $\hat{b}(E_t)$ , and  $\hat{b}(Z_y)$ .

**Fig.16:** Fast-particle fractions (fraction of particles detected at  $\theta=9^\circ-23^\circ$  with velocities greater than half the beam velocity) for  $^{36}\text{Ar}+^{197}\text{Au}$  collisions at  $E/A=110$  MeV. Solid points, open squares and open circles depict values determined for narrow cuts on the reduced impact parameters determined from  $N_C$ ,  $E_t$ , and  $Z_y$ ; star-shaped points represent simultaneous cuts on  $\hat{b}(N_C)$ ,  $\hat{b}(E_t)$ , and  $\hat{b}(Z_y)$ .

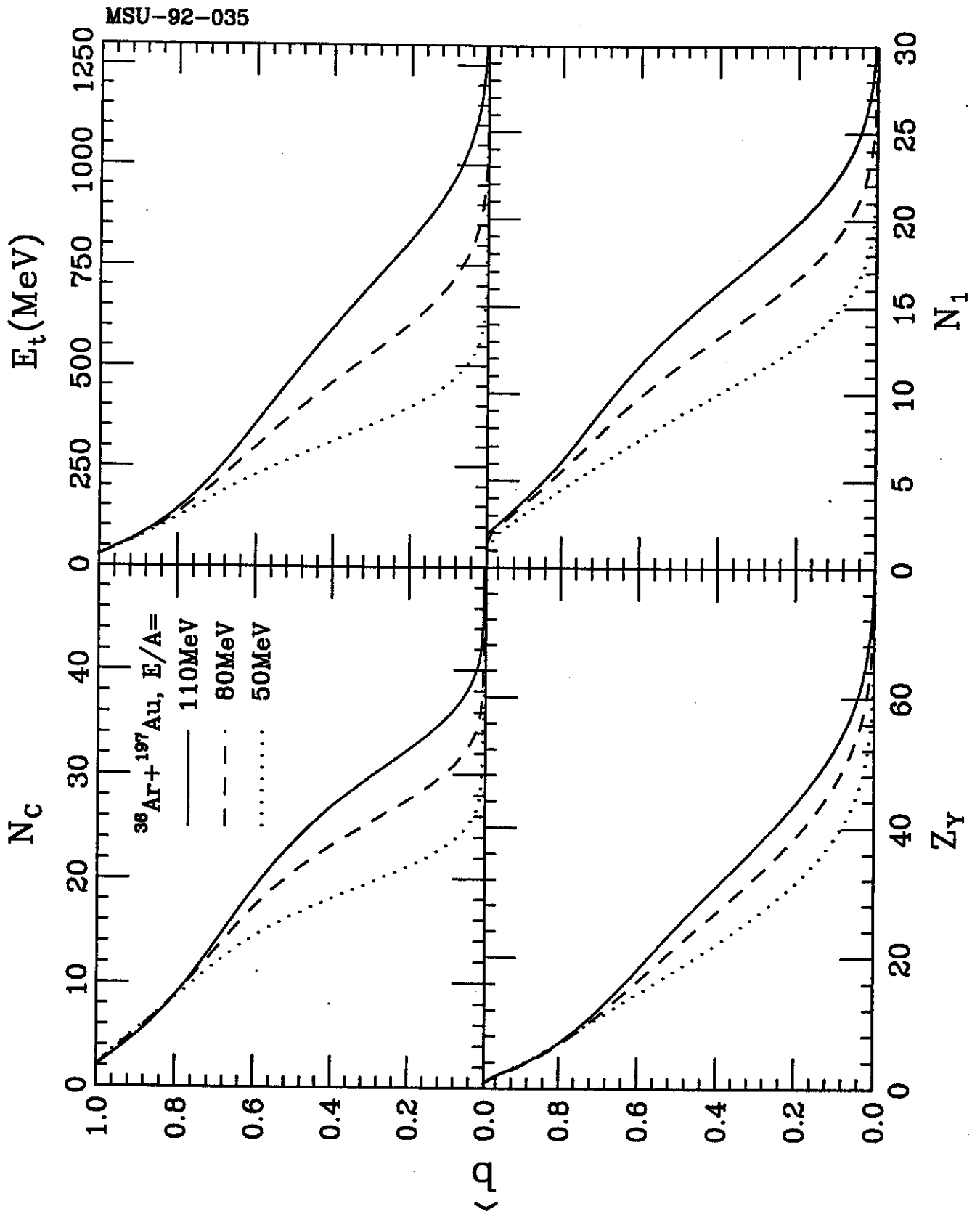


Fig 4

$^{36}\text{Ar} + ^{197}\text{Au}, E/A=110\text{MeV}$

MSU-92-039

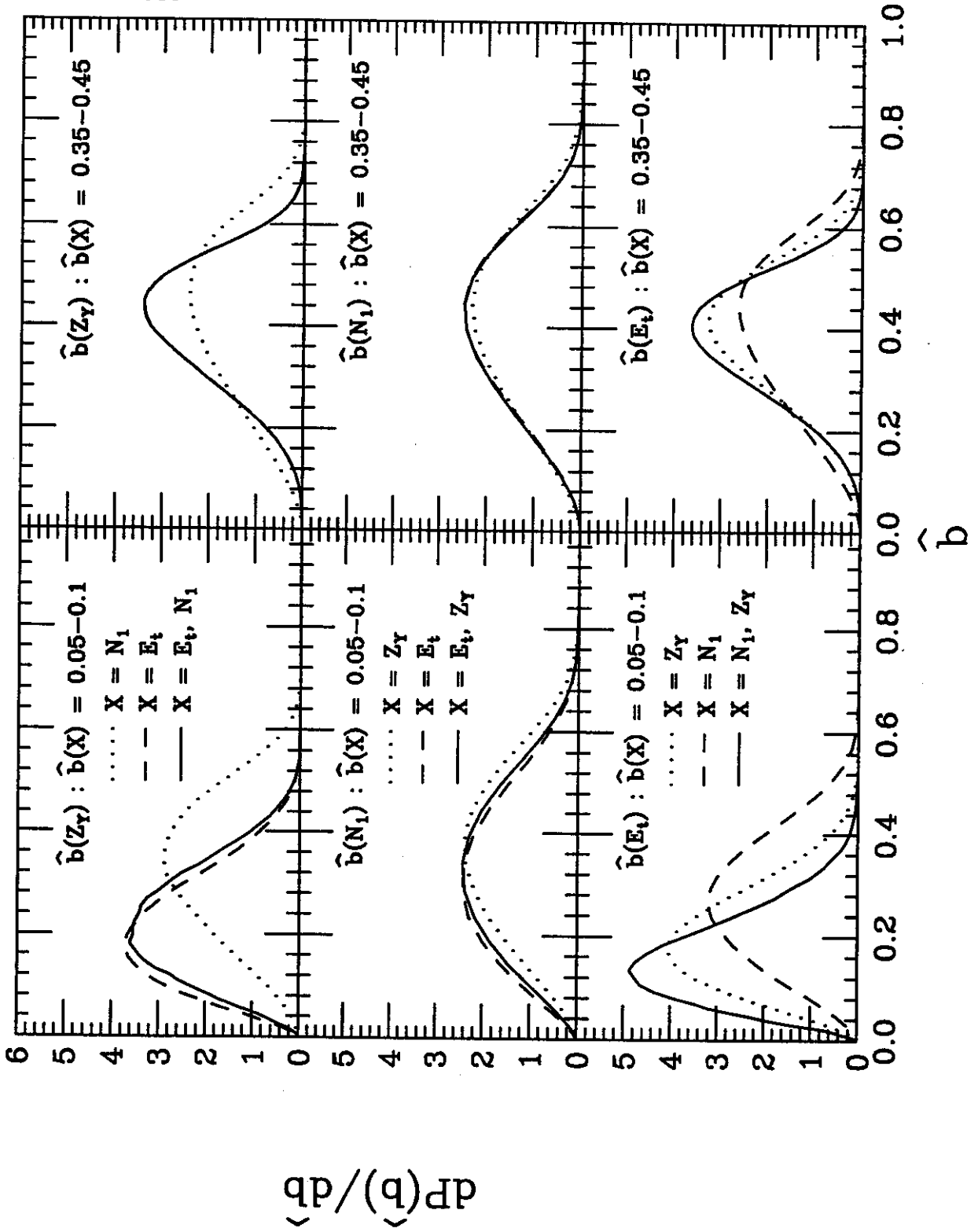


Fig.5

$^{36}\text{Ar} + ^{197}\text{Au}, E/A=50\text{MeV}$

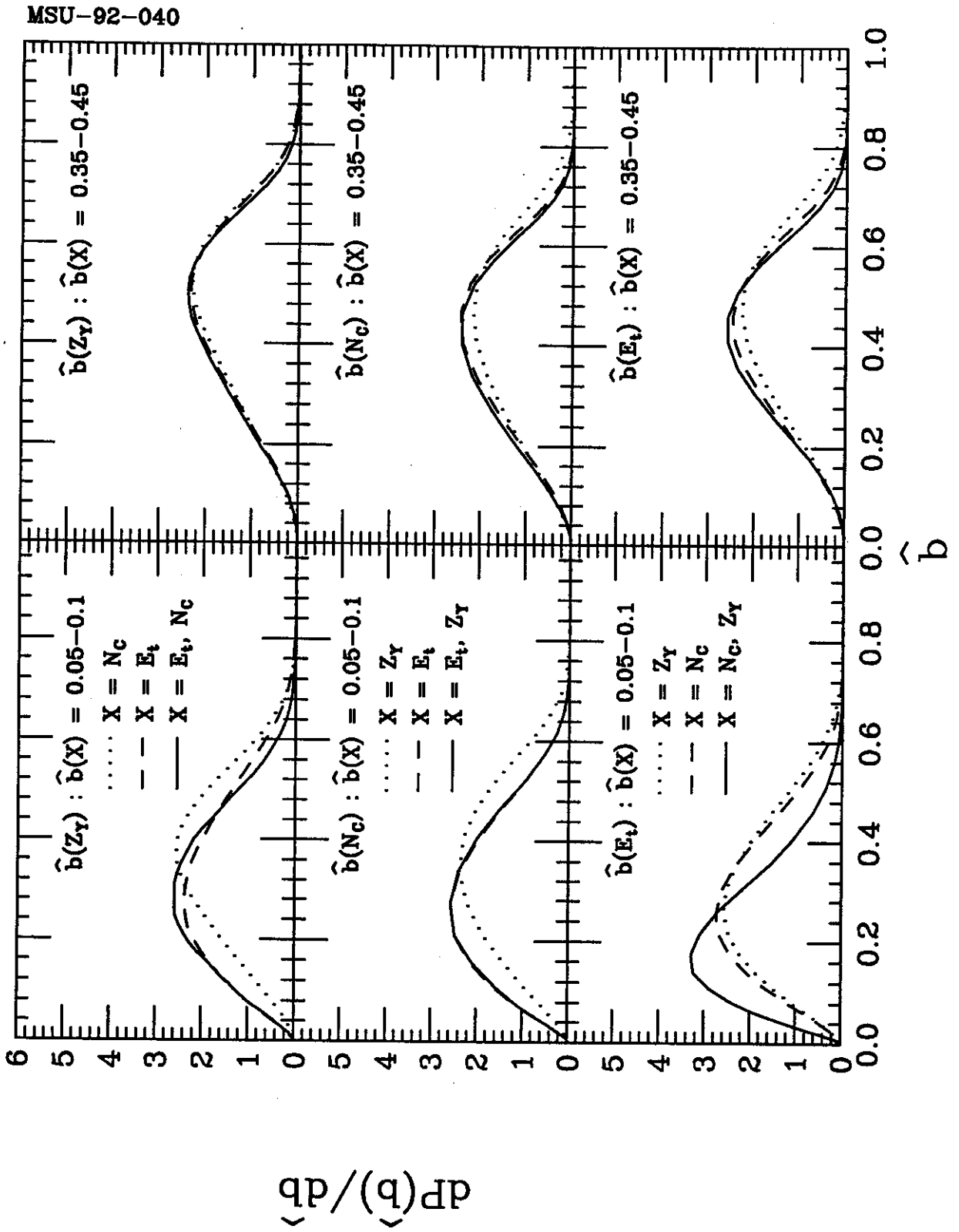


Fig. 6

$^{36}\text{Ar} + ^{197}\text{Au}, E/A=80\text{MeV}$

MSU-92-041

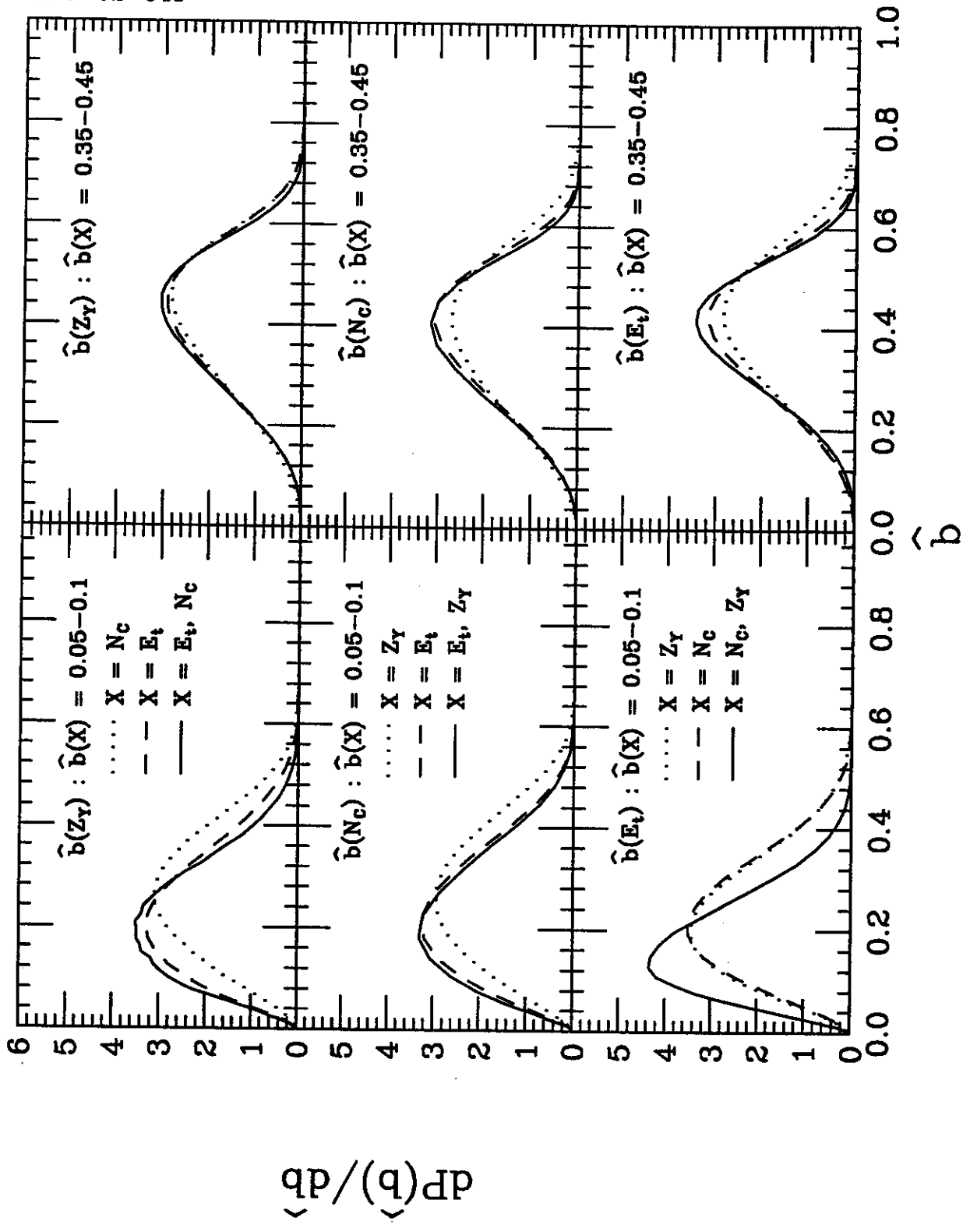


Fig. 7



$^{36}\text{Ar} + ^{197}\text{Au}, E/A=110\text{MeV}$

MSU-92-042

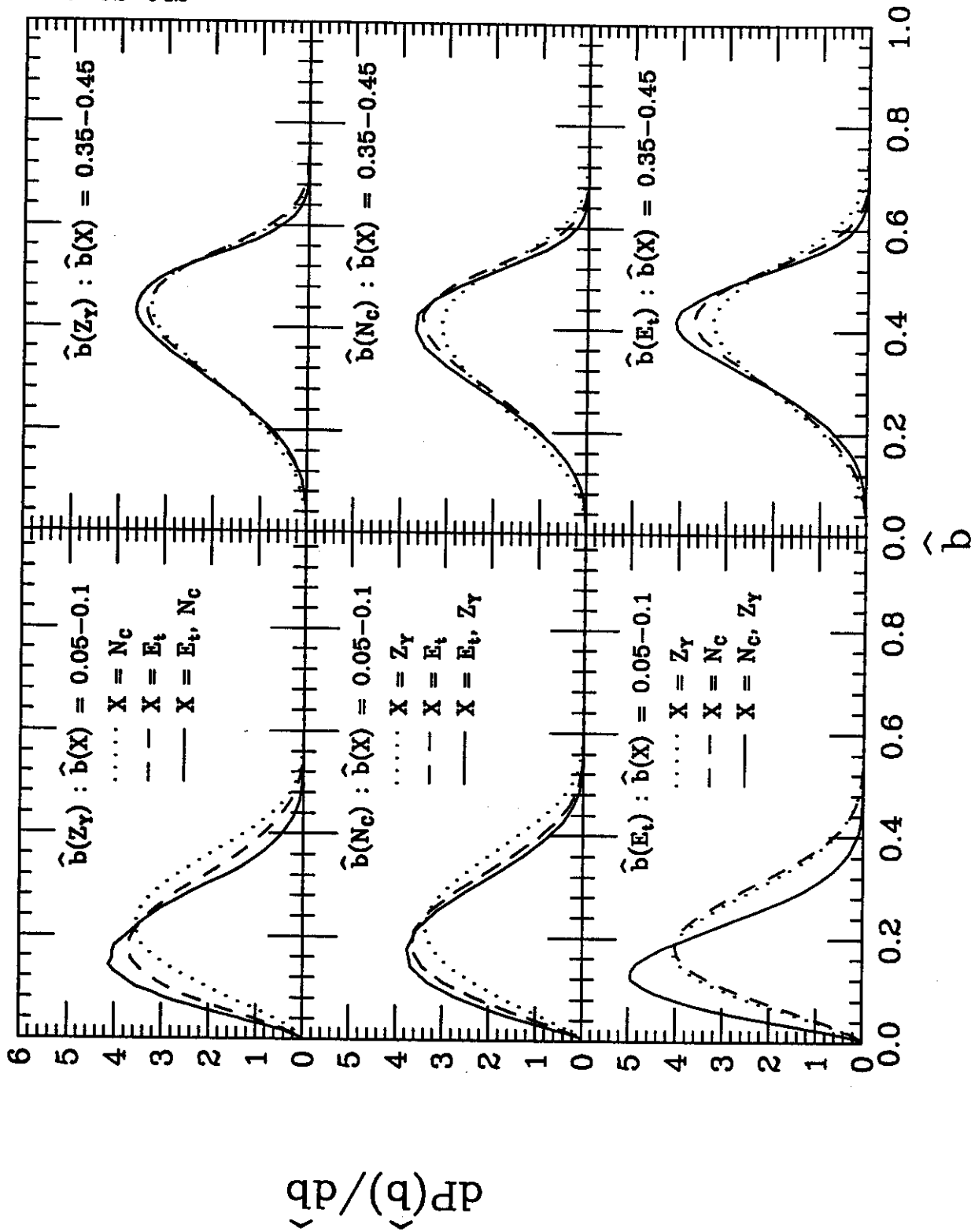
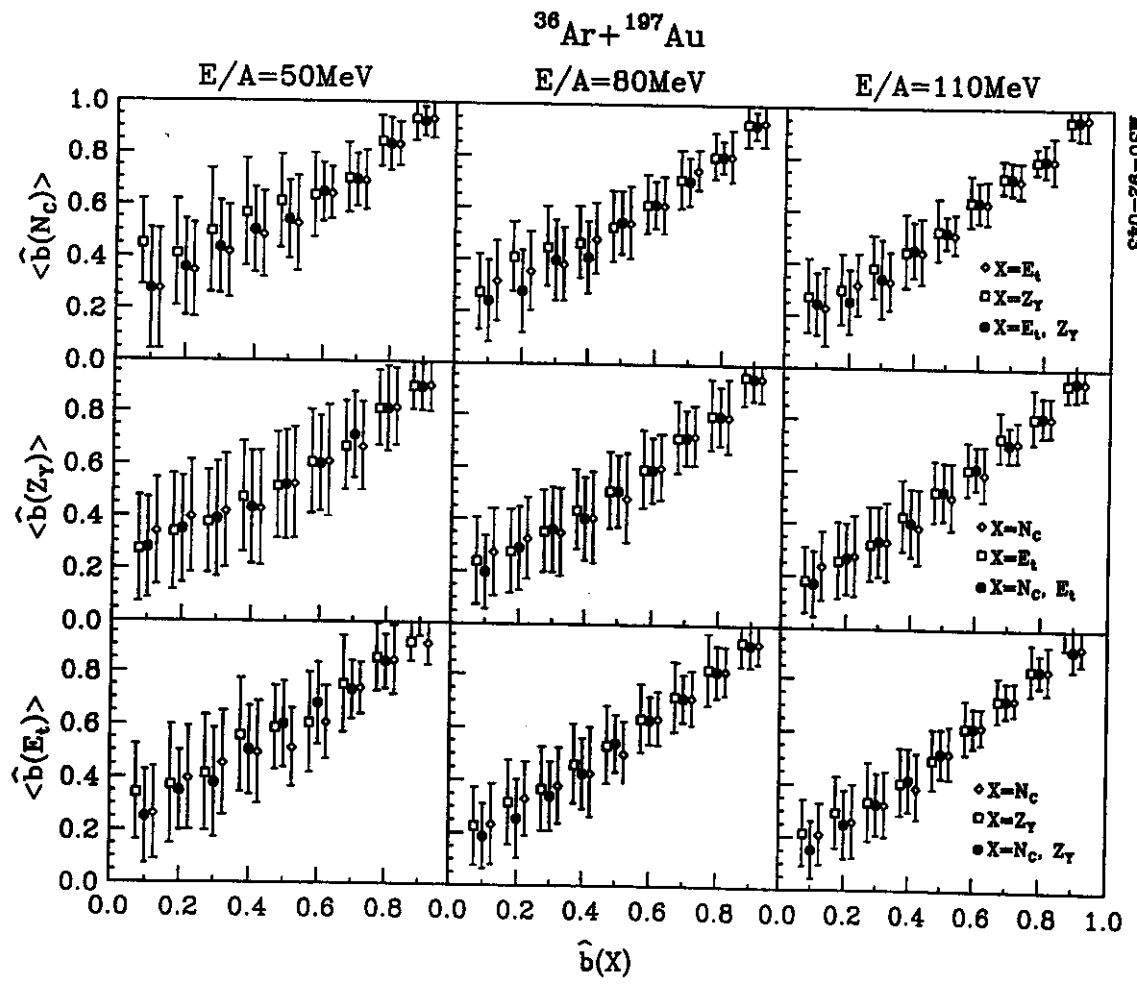


Fig. 8



MSU-92-043

Fig. 9

$^{36}\text{Ar} + ^{197}\text{Au}$ ,  $E/A = 50\text{MeV}$

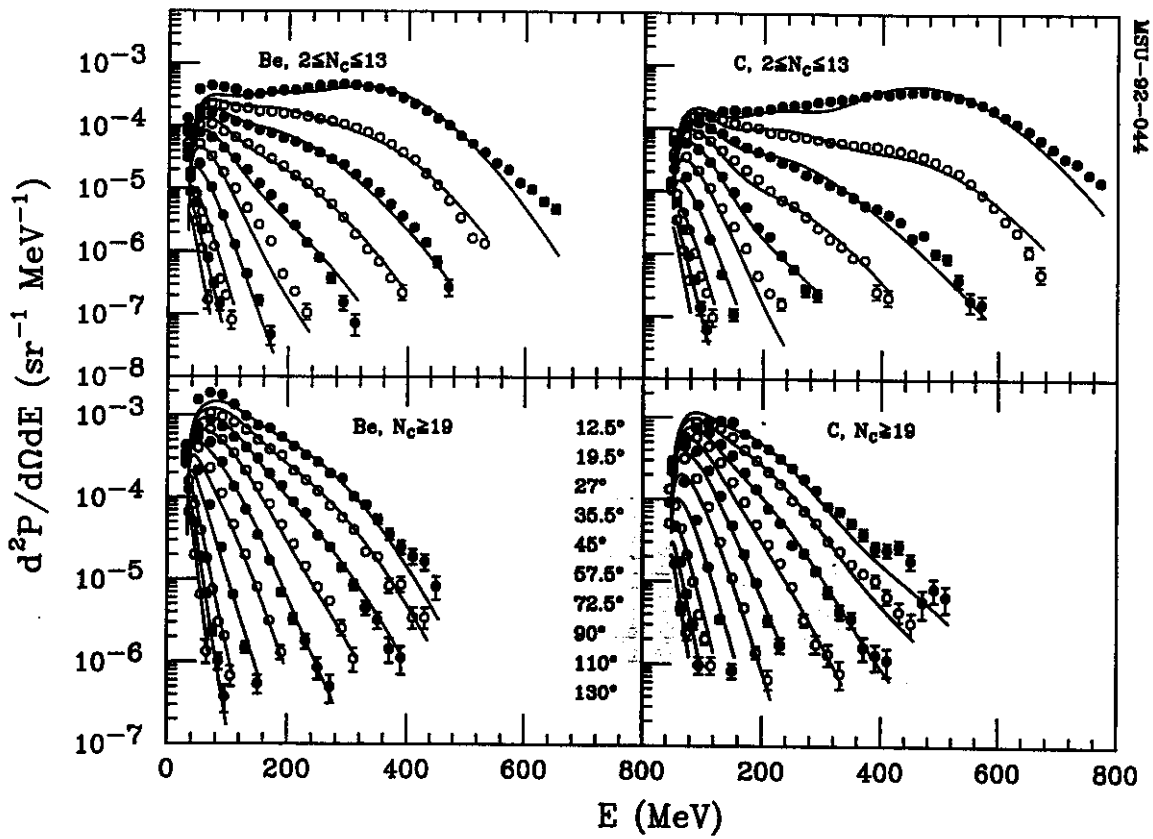


Fig.10

$^{36}\text{Ar} + ^{197}\text{Au}$ ,  $E/A = 80\text{MeV}$

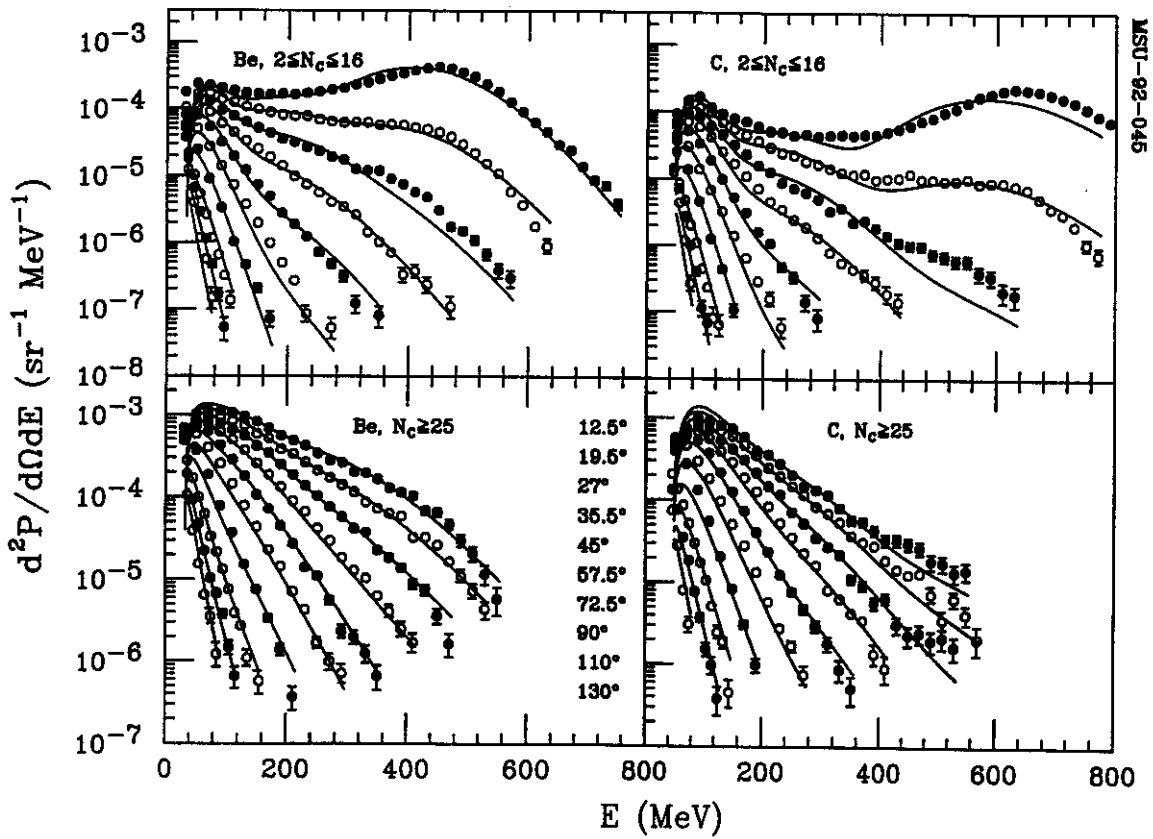


Fig. 11

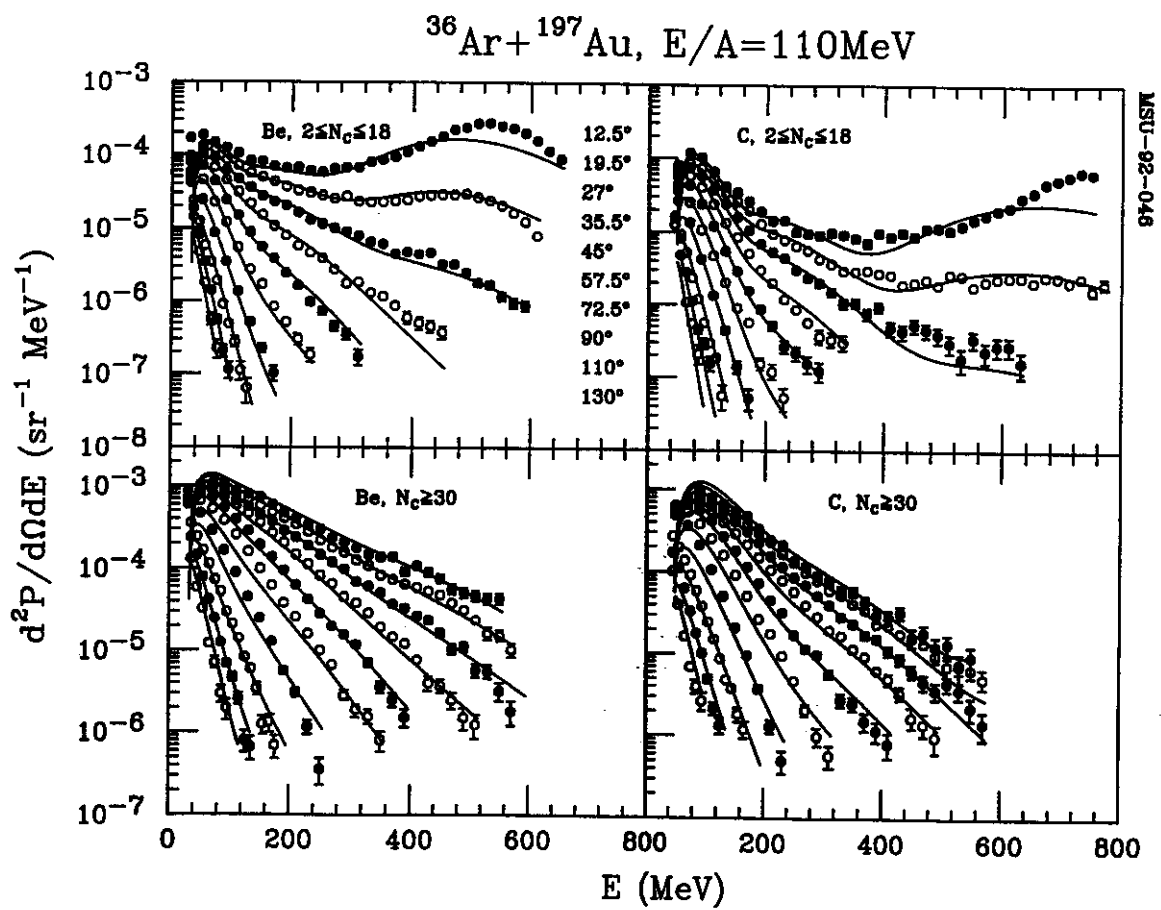


Fig. 12

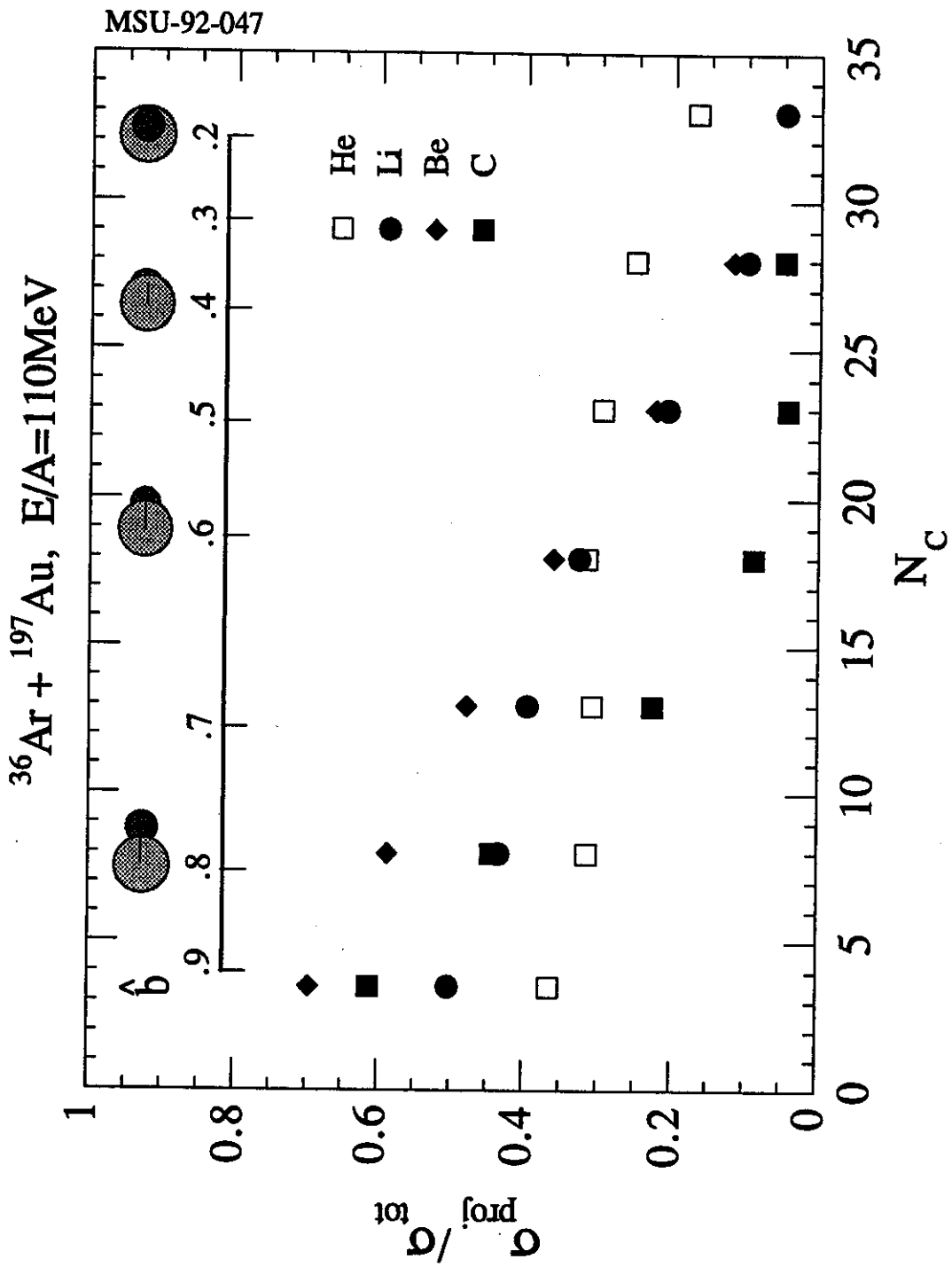


Fig. 13

$^{36}\text{Ar} + ^{197}\text{Au}, E/A = 50\text{MeV}$

MSU-92-04B

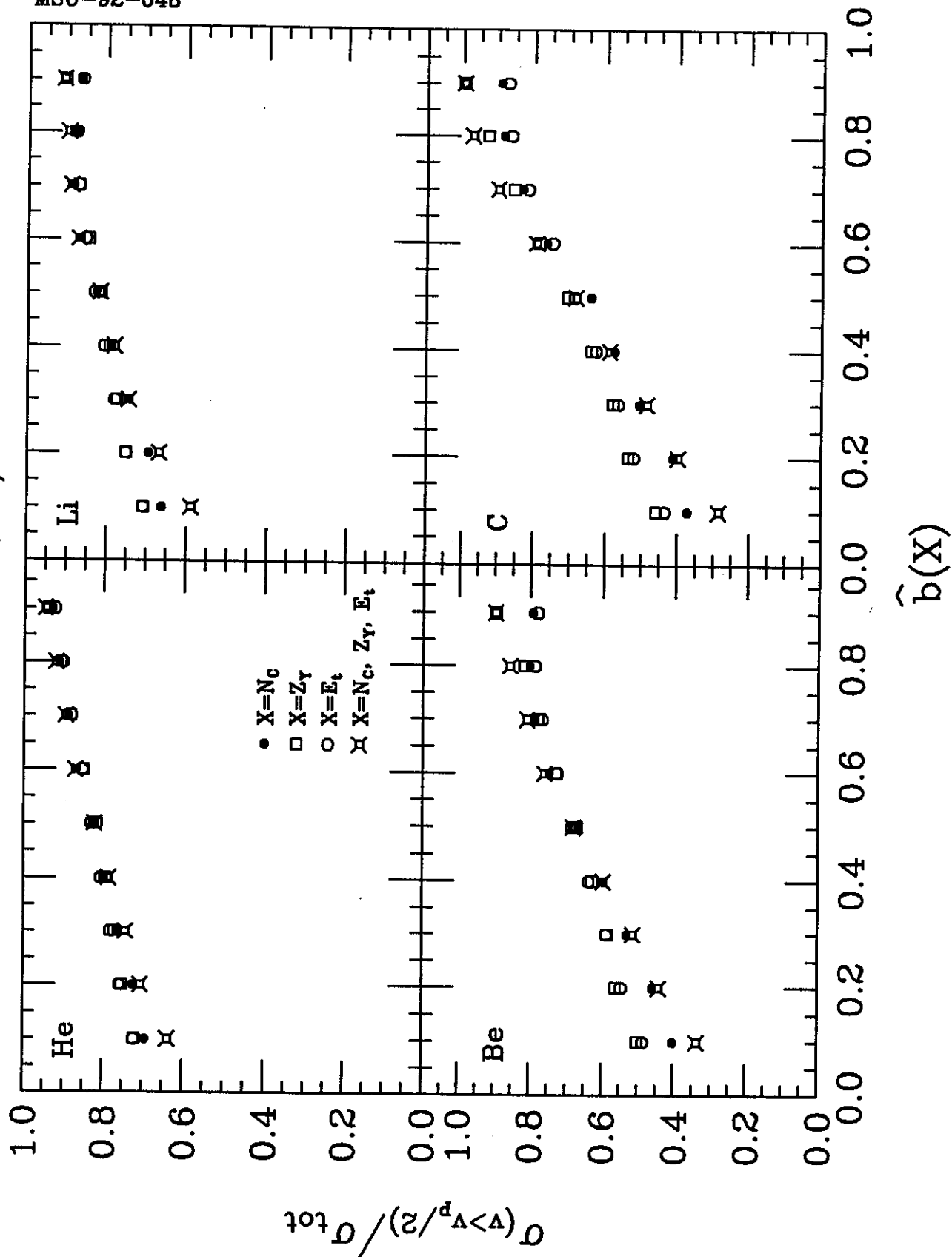


Fig. 14

$^{36}\text{Ar} + ^{197}\text{Au}, E/A = 80\text{MeV}$

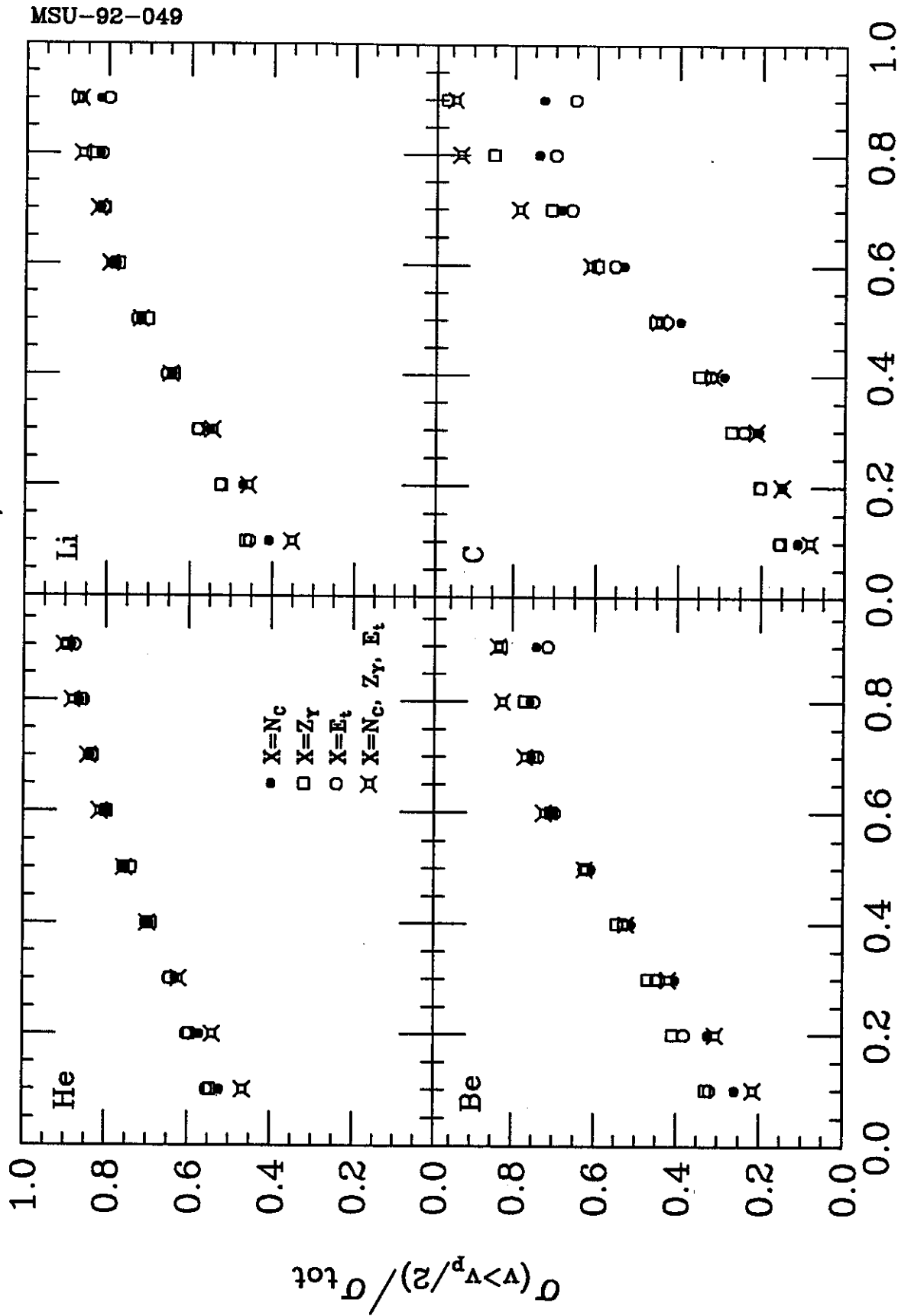


Fig. 15



$^{36}\text{Ar} + ^{197}\text{Au}, E/A = 110\text{MeV}$

MSU-92-050

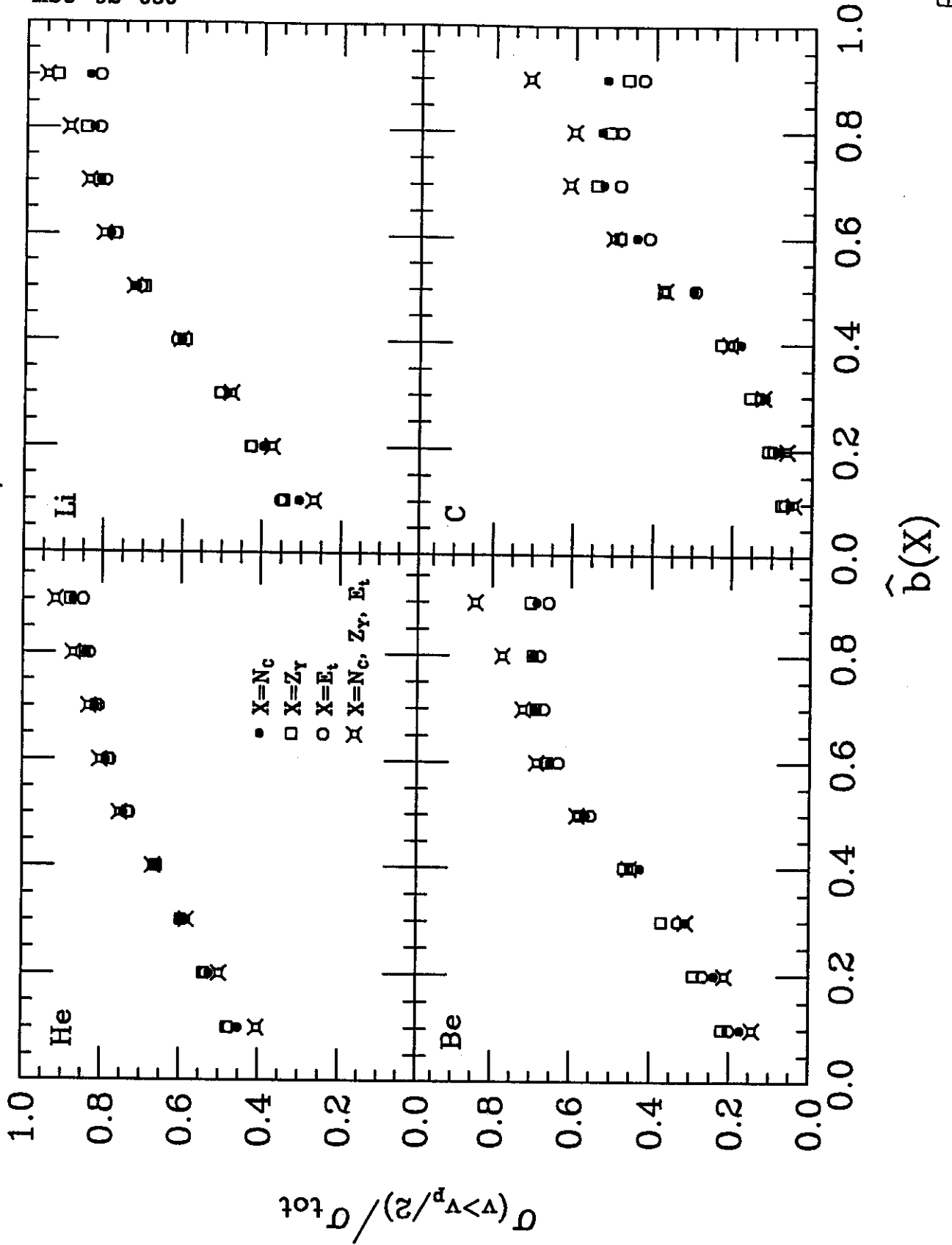


Fig. 16